Monthly Notices
of the
ROYAL ASTRONOMICAL SOCIETY

MNRAS **488,** 4663–4673 (2019)
Advance Access publication 2019 July 31

doi:10.1093/mnras/stz2054

The geometry of the gas surrounding the Central Molecular Zone: on the origin of localized molecular clouds with extreme velocity dispersions

Mattia C. Sormani [1]★ Robin G. Treß,[1] Simon C. O. Glover,[1] Ralf S. Klessen,[1,2] Ashley T. Barnes,[3] Cara D. Battersby,[4] Paul C. Clark [5] H. Perry Hatchfield[4] and Rowan J. Smith [6]

[1] *Universität Heidelberg, Zentrum für Astronomie, Institut für theoretische Astrophysik, Albert-Ueberle-Str. 2, 69120 Heidelberg, Germany*
[2] *Universität Heidelberg, Interdisziplinäres Zentrum für Wissenschaftliches Rechnen, Im Neuenheimer Feld 205, 69120 Heidelberg, Germany*
[3] *Argelander Institute for Astronomy, University of Bonn, Auf dem Hügel 71, D-53121 Bonn, Germany*
[4] *Department of Physics, University of Connecticut, 2152 Hillside Road,U-3046, Storrs, CT 06269, USA*
[5] *School of Physics and Astronomy, Queen's Buildings, The Parade, Cardiff University, Cardiff, CF24 3AA, UK*
[6] *Jodrell Bank Centre for Astrophysics, School of Physics and Astronomy, University of Manchester, Oxford Road, Manchester M13 9PL, UK*

Accepted 2019 July 13. Received 2019 June 23; in original form 2019 April 5

ABSTRACT

Observations of molecular gas near the Galactic Centre ($|l| < 10°$, $|b| < 1°$) reveal the presence of a distinct population of enigmatic compact clouds that are characterized by extreme velocity dispersions ($\Delta v > 100\,\mathrm{km\,s^{-1}}$). These extended velocity features are very prominent in the data cubes and dominate the kinematics of molecular gas just outside the Central Molecular Zone (CMZ). The prototypical example of such a cloud is Bania Clump 2. We show that similar features are naturally produced in simulations of gas flow in a realistic barred potential. We analyse the structure of the features obtained in the simulations and use this to interpret the observations. We find that the features arise from collisions between material that has been infalling rapidly along the dust lanes of the Milky Way bar and material that belongs to one of the following two categories: (i) material that has 'overshot' after falling down the dust lanes on the opposite side; (ii) material which is part of the CMZ. Both types of collisions involve gas with large differences in the line-of-sight velocities, which is what produces the observed extreme velocity dispersions. Examples of both categories can be identified in the observations. If our interpretation is correct, we are directly witnessing (a) collisions of clouds with relative speeds of $\sim 200\,\mathrm{km\,s^{-1}}$ and (b) the process of accretion of fresh gas onto the CMZ.

Key words: ISM: kinematics and dynamics – Galaxy: centre – Galaxy: kinematics and dynamics – galaxies: kinematics and dynamics.

1 INTRODUCTION

The geometry of the gas in the Central Molecular Zone (CMZ – defined here as the region at a radial distance $R \lesssim 200\,\mathrm{pc}$ from the Galactic Centre, or equivalently $|l| \lesssim 1.5°$) has been intensively studied in recent years (e.g. Molinari et al. 2011; Kruijssen, Dale & Longmore 2015; Henshaw et al. 2016; Sormani et al. 2018b). In contrast, the region immediately surrounding the CMZ has received relatively little attention. However, it is well known that the CMZ is not an isolated system but instead is strongly interacting with its surroundings. For example, the Galactic bar continuously drives a gas inflow into the CMZ, which strongly affects its dynamics and may even drive the observed turbulence of the CMZ (Sormani & Barnes 2019).

Among the most enigmatic features in the region surrounding the CMZ is a discrete population of extremely broad-lined ($\Delta v > 100\,\mathrm{km\,s^{-1}}$) compact clouds that are very prominent in molecular line data cubes (e.g. CO) in the region $|l| \leq 10°$ (Liszt 2006, 2008). These features dominate the kinematics of molecular gas just outside the CMZ. The prototypical example is Bania Clump 2 (Stark & Bania 1986). Despite their enormous velocity dispersion, these puzzling features are confined to a narrow longitude range. Similar features are not found anywhere else in the Galaxy. In this paper, we will refer to these features as extended velocity features (EVFs) on account of their large velocity dispersions. We give a brief summary of the observational properties of the EVFs in Section 2.

★ E-mail: mattia.sormani@alumni.sns.it

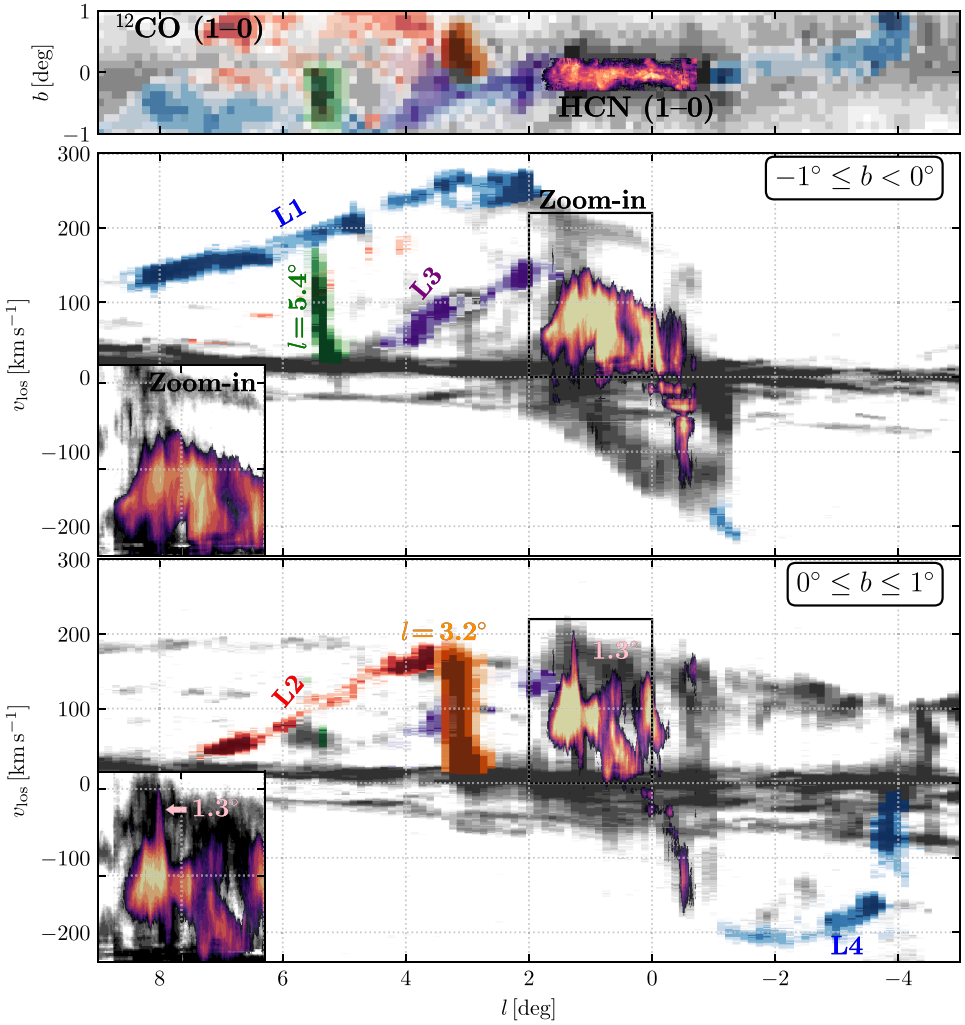

Figure 1. Molecular emission from the inner Galaxy. Some of the most prominent EVFs ($l = 1.3^\circ$, $l = 3.2^\circ$ aka Bania Clump 2, and $l = 5.4^\circ$) and the dust lane–like features identified by Liszt (2008) (L1 to L4) are indicated. The grey background shows the ^{12}CO $J = 1 \rightarrow 0$ data from Bitran et al. (1997) (in the main panels) and Oka et al. (1998) (in the zoom-in panels). The $l = 5.4^\circ$, $l = 3.2^\circ$, and L1 to L4 features are highlighted in the CO data. The magma colour scale in the centre shows HCN from the data of Jones et al. (2012). The HCN data cover only the region $-0.7 < l < 1.8^\circ$, $-0.3 < b < 0.2^\circ$, and $-300 < v < 300\,\mathrm{km\,s^{-1}}$. The $l = 1.3^\circ$ feature is visible in the HCN data and is indicated with an arrow.

Several possible interpretations of the EVFs have been put forward in the literature:

(a) They are gaseous structures extended in space that happen to coincidentally lie parallel to the line of sight (e.g. Stark & Bania 1986; Boyce, Cohen & Dent 1989; Lee et al. 1999; Baba, Saitoh & Wada 2010). Such interpretations suffer from the 'fingers of god' effect, i.e. they assume that we are at a special location in the universe in which these structures happen to point toward us.

(b) Some of them have been interpreted as the footprints of giant magnetic loops caused by the Parker (1966) instability near the Galactic Centre (Fukui et al. 2006; Fujishita et al. 2009; Machida et al. 2009; Torii et al. 2010; Suzuki et al. 2015; Riquelme et al. 2018).

(c) Some of them have been interpreted as evidence for the presence of intermediate-mass black holes (IMBH) (Oka et al. 2016, 2017; Takekawa et al. 2019a,b).

(d) They are lumps that are just about to cross the dust lanes of the Milky Way bar (Fux 1999, see also Liszt 2006, 2008).

In this paper, we show that features similar to the observed ones arise naturally in simulations of gas flow in a barred potential. We then use the insight gained from the simulations to interpret the observations. The paper is structured as follows. In Section 2, we briefly review the observations and the key properties that characterize the EVFs. In Section 3, we describe the numerical set-up of our simulations. In Sections 4 and 5, we discuss our results and interpret the observations. Finally in Section 6, we sum up.

2 OBSERVATIONS

Here we briefly review the observational data. A more detailed analysis can be found, for example, in Liszt (2006, 2008) and Oka et al. (2012) for CO, Boyce & Cohen (1994) for OH, Longmore et al. (2017) for NH_3, and McClure-Griffiths et al. (2012) for HI.

Fig. 1 shows molecular line emission from the inner Galaxy. The three most prominent EVFs are highlighted: these are the $l = 5.4^\circ$, the $l = 3.2^\circ$ (also known as Bania Clump 2), and the $l = 1.3^\circ$

features. Other, less prominent EVFs can be found throughout the inner regions of our Galaxy (see references above).

Also highlighted are the dust lane features L1 to L4. These are not EVFs but are often linked to them in (l, b, v) space (see Property vi below). The 'dust lane' terminology is used here for historical reasons despite these features being primarily (but not exclusively) detected in gas. The terminology originally comes from observations of external barred galaxies such as NGC 1300 or NGC 5383 in which one can see 'the presence of two dust lanes leaving the nucleus one on each side of the bar and extending into the spiral arms' (Sandage 1961). After it was realized that the MW is a barred galaxy, the features L1 and L4 were identified as the dust lanes of the MW bar (Fux 1999), and the 'dust lane' terminology was maintained despite the fact that they were initially observed in HI and CO emission and not from dust emission/extinction. Subsequent work has identified the L1 and L4 features also from the dust (Marshall et al. 2008). Beyond the two main dust lane features L1 and L4, Liszt (2008) determined the presence of the two additional secondary dust lane features L2 and L3 using CO emission. As we will see later in the paper, the presence of multiple dust lanes also occurs in our simulations.

The key properties that characterize the EVFs are:

(i) They are extremely broad-lined, with velocity dispersions of up to 200 km s^{-1} when observed at low resolution.

(ii) They are compact, so they are very localized in the (l, b) plane (the typical extensions of the largest EVFs are Δl, $\Delta b \sim 0.5^\circ$).

(iii) They are usually more extended in latitude than in longitude. So they are typically elongated perpendicularly to the Galactic plane.

(iv) They are predominantly found in the ($v > 0$, $l > 0$) and ($v < 0$, $l < 0$) quadrants of the (l, v) plane, although a few of them are found in the other two quadrants as well.

(v) They never extend beyond the terminal velocity curve (TVC)[1] at their value of longitude.

(vi) Some of them are clearly connected to some dust lane–like features associated with the Galactic bar (see, for example, how the $l = 5.4^\circ$ EVF connects L1 to L3 or how the $l = 3.2^\circ$ EVF is connected to L2, see also Liszt 2008).

(vii) Some of them (e.g. Bania's Clump 2) show sharp HI emission profiles on one side (McClure-Griffiths et al. 2012).

(viii) When observed at very high resolution, they typically break up into multiple kinematic sub-components with strong velocity gradients (see, for example, Liszt 2006, which resolved the internal velocity structure of several EVFs and fig. 30 of Longmore et al. 2017, which shows the complicated velocity structure of Bania Clump 2 in NH_3).

Successful theoretical models should be able to reproduce the above properties.

3 NUMERICAL SET-UP

Our numerical set-up is the same as that of Sormani et al. (2018b) except for a few differences. Therefore, we provide here only a brief recap and state the differences from these previous simulations and refer the reader to Section 3 of Sormani et al. (2018b) and references therein for a more detailed description.

[1]The TVC at $l > 0$ ($l < 0$) is defined as the maximum (minimum) value of line-of-sight velocity at which the bulk of the emission from the Galactic disc is found, i.e. it is the curve that defines the envelope of the latitude-integrated (l, v) diagram (see, for example Binney & Merrifield 1998, Chapter 9).

3.1 Hydrodynamic code

The simulations are three-dimensional (3D) and the gas is assumed to flow in a multicomponent external barred potential $\Phi(\boldsymbol{x}, t)$, which is constructed to fit the properties of the Milky Way (see next section and Appendix A). The gas self-gravity and magnetic fields are neglected.

We use the moving-mesh code AREPO (Springel 2010), modified to treat the chemical evolution of the interstellar gas. The code solves the equations of fluid dynamics:

$$\frac{\partial \rho}{\partial t} + \nabla \cdot (\rho \boldsymbol{v}) = 0, \tag{1}$$

$$\frac{\partial (\rho \boldsymbol{v})}{\partial t} + \nabla \cdot (\rho \boldsymbol{v} \otimes \boldsymbol{v} + P\mathbf{I}) = -\rho \nabla \Phi, \tag{2}$$

$$\frac{\partial (\rho e)}{\partial t} + \nabla \cdot [(\rho e + P)\boldsymbol{v}] = \dot{Q} + \rho \frac{\partial \Phi}{\partial t}, \tag{3}$$

where ρ is the gas density, $\boldsymbol{v}$ is the velocity, P is the thermal pressure, $\mathbf{I}$ is the identity matrix, $e = e_{\rm therm} + \Phi + \boldsymbol{v}^2/2$ is the energy per unit mass, and $e_{\rm therm}$ is the thermal energy per unit mass. We adopt the equation of state of an ideal gas, $P = (\gamma - 1)\rho e_{\rm therm}$, where $\gamma = 5/3$ is the adiabatic index.

We account for the chemical evolution of the gas using an updated version of the NL97 chemical network from Glover & Clark (2012), which itself was based on the work of Glover & Mac Low (2007a,b) and Nelson & Langer (1997). With this network, we solve for the non-equilibrium abundances of H, H_2, H^+, C^+, O, CO, and free electrons. An extensive description of the network is given in Section 3.4 of Sormani et al. (2018b) and in the interests of brevity, we do not repeat it here.

The term $\dot{Q}$ in equation (3) contains the contributions of the radiative and chemical processes that can change the internal energy of the system ($\dot{Q} = 0$ for an adiabatic gas). It includes (i) a cooling function that depends on the instantaneous chemical composition of the gas (Glover et al. 2010; Glover & Clark 2012); (ii) the heat absorbed or released in the most important chemical processes that occur in the interstellar medium, which are tracked in real time by the chemical network; and (iii) external heating sources that represent the average interstellar radiation field (ISRF) and cosmic ray ionization rate. The strength of the ISRF is set to the standard value G_0 measured in the Solar neighbourhood (Draine 1978) diminished by a local attenuation factor that depends on the amount of gas present within 30 pc of each computational cell. This attenuation factor is introduced to account for the effects of dust extinction and H_2 self-shielding and is calculated using the TREECOL algorithm described in Clark, Glover & Klessen (2012). The cosmic ray ionization rate is fixed to $\zeta_{\rm H} = 3 \times 10^{-17}$ s^{-1} (Goldsmith & Langer 1978). These values correspond to the 'low' simulation of Sormani et al. (2018b). We have shown in that paper that the strength of the ISRF mainly controls the amount of molecular gas but makes little difference to the dynamics. Indeed, even if the ISRF field is a factor of a 1000 higher than in the Solar neighbourhood (Clark et al. 2013), the sound speed of the molecular gas comes nowhere close to the values of $c_{\rm s} = 5$–10 km s^{-1}, which would be needed to significantly affect the dynamics of the gas (Sormani, Binney & Magorrian 2015a). Hence, the results of the present paper are not affected by the strength of the assumed ISRF.

3.2 Differences between Sormani et al. (2018b) and the present paper

The main difference between the simulations in Sormani et al. (2018b) and the one used in this paper is that we modified the gravitational potential of the bar so that the size of the nuclear ring that naturally forms in the simulation matches the observed size of the CMZ (it was a factor of ∼2 too large in the previous simulations). In general, the size of this ring is controlled by (i) the parameters of the gravitational potential, mainly the bar strength and the bar pattern speed (e.g. Sormani et al. 2018a, and references therein) and (ii) the effective sound speed of the gas (see, for example, fig. 1 of Sormani et al. 2015a). Since the sound speed of the gas is fixed by our treatment of the heating and cooling of the ISM and the pattern speed of the gas is independently constrained to be $\Omega_p = 40\,\mathrm{km\,s^{-1}\,kpc^{-1}}$ (e.g. Sormani, Binney & Magorrian 2015b; Portail et al. 2017; Sanders, Smith & Evans 2019), we have increased the strength of the bar (compatibly with known observational constraints) to achieve the desired result of a smaller ring. The gravitational potential and the resulting rotation curve are described in detail in Appendix A.

The second difference is that we increased the resolution. The resolution in the simulation is determined by the condition that cells approximately have the same mass (so that denser gas has a higher spatial resolution). The system of mass refinement present in AREPO ensures that this condition is satisfied by splitting cells whose mass becomes greater than twice this target mass and merging cells whose mass is too low. Here we use a target resolution of $25\,\mathrm{M_\odot}$ per cell, while in Sormani et al. (2018b) we used a target resolution of $100\,\mathrm{M_\odot}$.

The last difference is in the initial density profile of the gas. In Sormani et al. (2018b), the initial density distribution was approximately uniform inside a cylindrical slab of radius 10 kpc and half-height 1 kpc, with the addition of some small random noise. Here instead we initialize the density according to the following axisymmetric density distribution:

$$\rho(R,z) = \frac{\Sigma_0}{4z_\mathrm{d}} \exp\left(-\frac{R_\mathrm{m}}{R} - \frac{R}{R_\mathrm{d}}\right) \mathrm{sech}\left(\frac{z}{2z_\mathrm{d}}\right)^2, \quad (4)$$

where (R, ϕ, z) denote standard cylindrical coordinates, $z_\mathrm{d} = 85\,\mathrm{pc}$, $R_\mathrm{d} = 7\,\mathrm{kpc}$, $R_\mathrm{m} = 1.5\,\mathrm{kpc}$, $\Sigma_0 = 50\,\mathrm{M_\odot\,pc^{-2}}$, and we also have cut our disc so that $\rho = 0$ for $R \geq 5\,\mathrm{kpc}$. This profile better matches the observed radial distribution of gas in the Galaxy (Kalberla & Dedes 2008; Heyer & Dame 2015). The initial density distribution is very smooth and we do not include any random noise. Despite this smoothness of the initial conditions, the gas flow in the bar region ends up being unsteady and turbulent because of the processes described in section 4 of Sormani et al. (2018b).

4 RESULTS

Fig. 2 shows a snapshot of our simulation at $t = 178\,\mathrm{Myr}$. The top row shows the HI and CO surface density in the (x, y) plane, while the bottom row shows the corresponding projections in the (l, v) plane. To produce these projections, we bin each AREPO cell as a point in the (l, v) plane with a weight proportional to the mass of the component of interest (HI or CO, as appropriate) and inversely proportional to the square of its distance from the Sun, as discussed in more detail in section 3.6 of Sormani et al. (2018b). These projections assume that the gas is optically thin to HI and CO line emission, but accounting more accurately for line opacities would only change the strength of the emission and not its distribution in the (l, v) plane. Fig. 3 shows the correspondence between top down and projection plots in more detail, with labels that identify some of the interesting features.

Several features that resemble the observed EVFs can be identified in the various (l, v) projections. A particularly prominent one is the red feature at $l \simeq 3^\circ$ labelled V1 in Fig. 3. This feature has an extreme velocity dispersion ($\Delta v \sim 200\,\mathrm{km\,s^{-1}}$) but is very localized in real (x, y) space (it all originates from the small red patch visible in the top left-hand panel of Fig. 3). This is precisely the main property that characterizes the observed EVFs (see Section 2). The V1 feature connects the dust lane features D1 and D2 (see labels in Fig. 3). This is remarkably similar to what is observed for the EVF at $l \simeq 5.4^\circ$ in Fig. 1, which connects the main observed dust lane L1 to the secondary dust lane L3.

Inspection of the velocity fields in Figs 3 and 4 reveals the origin of the feature V1. It originates as gas on the feature O1 crashes into the dust lane feature D1. The feature O1 is gas that has fallen along the dust lane on the opposite side, touched and brushed the CMZ, and then continued its course until it crashed into the middle of feature D1.[2] When the feature O1 comes in contact with feature D1, the two have enormously different velocities. The signature of this collision in the (l, v) plane is the extreme velocity dispersion that characterizes the feature V1.

Fig. 3 also shows the presence of several further features with high-velocity dispersion at negative longitudes. These are coloured green. These features originate with a similar mechanism as the feature V1 discussed above. They look more crowded in the (l, v) plane partly on account of projection effects (they are on the far side of the Galaxy). The production of the EVFs is a stochastic process in the simulation on account of the unsteady and turbulent flow that develops due to the processes described in section 4 of Sormani et al. (2018b).

A second type of broad-lined features that have a somewhat different origin than the ones described above also appear during the course of the simulation. Fig. 5 shows an example of this second type of EVF. It is labelled V2 in the figure. This second type of feature originates as material that has been falling along the dust lanes crashes into the CMZ. The dense material in the CMZ typically has velocities much lower than those of the dust lanes, so when they collide they produce very broad-lined features like V2 in the figure. This feature has much in common with the observed EVF at $l = 1.3^\circ$ (see Fig. 1).

5 DISCUSSION

The results in the previous section suggest that at least some (perhaps most) of the EVFs found in the observations originate from collisions. These typically involve gas falling along the dust lanes that crashes with material with very different line-of-sight velocities. Our simulations show that this occurs naturally when gas flows in a barred potential and cannot be avoided: our initial conditions are prepared ensuring that the gas is as calm as possible (they are very smooth, symmetric, and do not include any random

[2]Using high-sensitivity CO data, Mizuno & Fukui (2004) have identified what might be the observational counterpart of the overshooting feature O1 (see crosses in their fig. 3). This feature seems to connect to the $l = 5.4^\circ$ feature in the 3D (l, b, v) space in a manner very similar to how the O1 feature connects to the V1 feature in our simulations. This, however, needs to be confirmed by future observations.

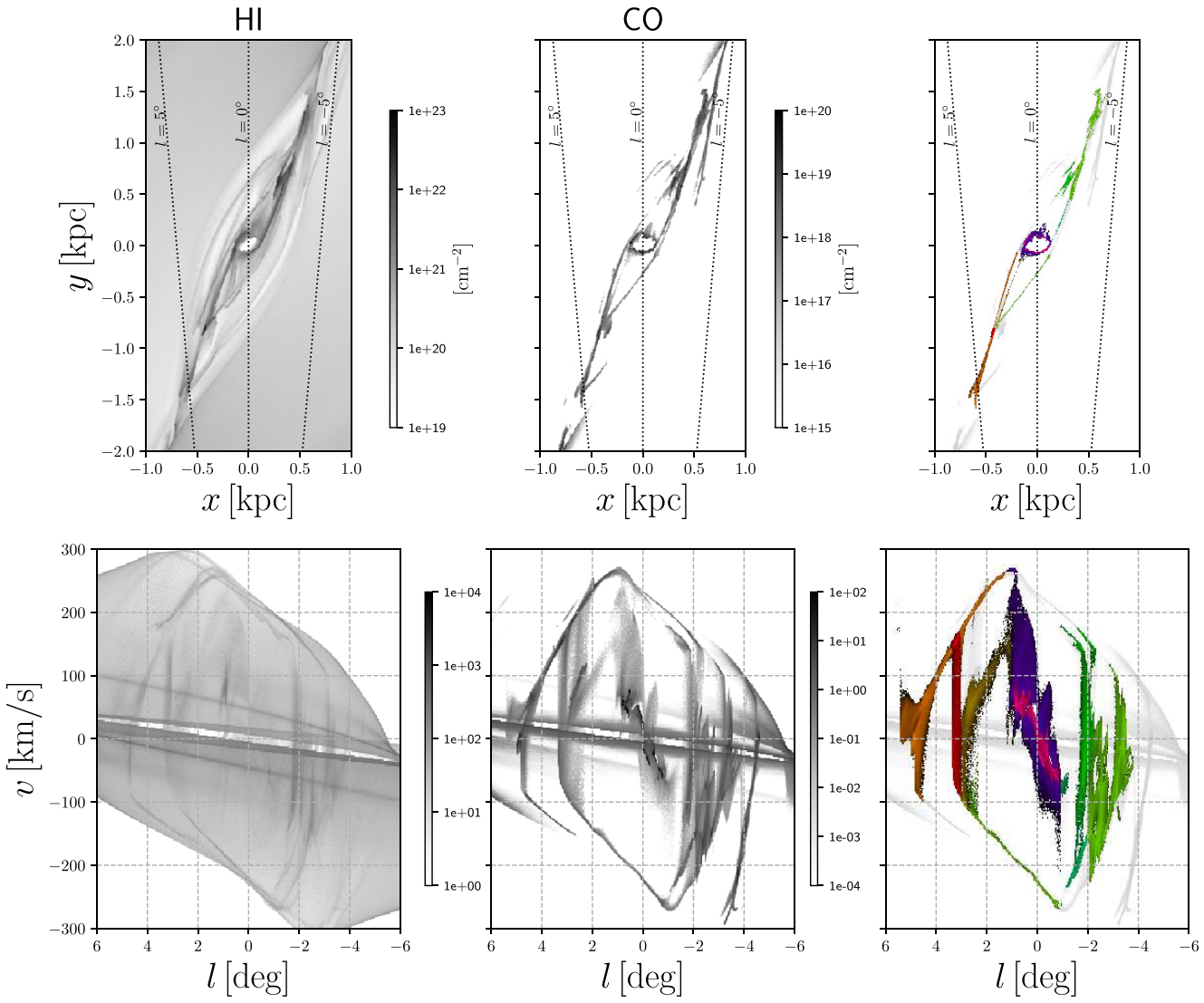

Figure 2. The snapshot of our simulation at $t = 178$ Myr. *Top row*: surface density of gas in the (x, y) plane. *Bottom row:* corresponding projections in the (l, v) plane in the optically thin approximation and assuming that the angle between the Sun-GC line and the major axis of the bar is $\phi = 20°$ (Bland-Hawthorn & Gerhard 2016). The left and middle column show HI and CO, respectively, as calculated by the chemical network included in the simulation. The right column shows a colour-coded map on top of the CO emission, allowing one to identify corresponding structures in the (x, y) and (l, v) views. A movie showing a 3D visualization of the snapshot shown in this figure can be downloaded from https://doi.org/10.7910/DVN/XFDYY7/0EEVVX. Movies showing the time evolution of the total gas density in the simulations on large scales and zooming-in onto the CMZ can be downloaded from https://doi.org/10.7910/DVN/XFDYY7/GUCB8W and https://doi.org/10.7910/DVN/XFDYY7/GD1R6S, respectively.

noise), yet such collisions develop spontaneously. This happens even in the absence of any form of stellar feedback.[3]

The EVFs occur frequently in the simulations although perhaps at any given time there are somewhat fewer of them in a synthetic (l, v) diagram than in its observational counterpart. This is probably a consequence of the fact that we have tried to keep the gas flow as smooth as possible, while in the real Galaxy more collisions should be expected on account of the facts that the initial conditions are most likely not smooth and that additional processes contribute to produce more unsteadiness and turbulence (stellar feedback, perturbations from satellite galaxies that punch through the MW disc, etc.). Thus, our simulations provide a lower limit on the number of EVF-producing collisions that might be expected in the real Galaxy.

Our interpretation naturally explains most of the key observational properties listed in Section 2. Property (i) is satisfied because this is the property by which we select features in the simulation to compare to the observed EVFs. Property (ii) is satisfied because the collision sites have limited extension in real (x, y) space, so the features are localized in the (l, b) plane. Property (iv) is satisfied because collisions in the simulations happen preferentially in the two quadrants ($l > 0$, $v > 0$) and ($l < 0$, $v < 0$), although not exclusively (see, for example, the green material in Fig. 3). Property

[3]Indeed, the gas flow in a barred potential is inevitably unsteady and turbulent (Sormani et al. 2018b). This is well illustrated, for example in the top left-hand panel in Fig. 2, which shows that inside the bar region the flow is structured and unsteady, in striking contrast with the flow just outside the bar region, which is extremely smooth and steady.

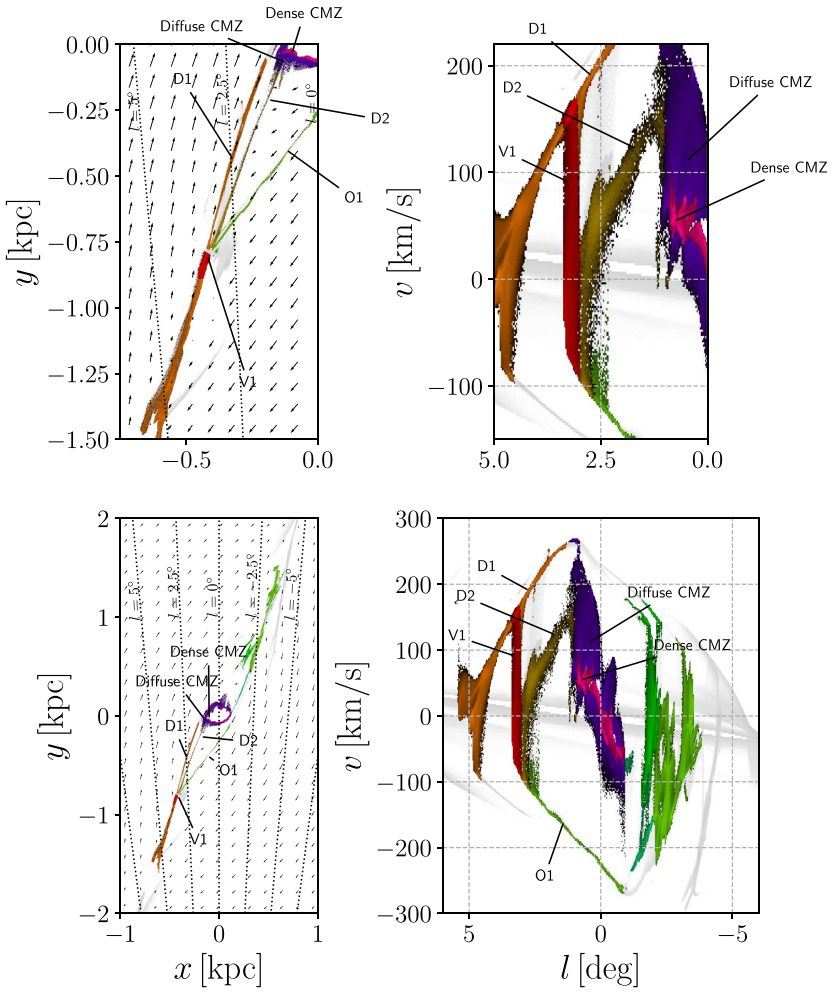

Figure 3. Features in the (x, y) plane and their projection to the (l, v) plane for the simulation snapshot at $t = 178$ Myr. The top panels are zoom-ins of the bottom panels. Arrows in the left-hand panels show the velocity field in the rotating frame of the bar. Labels mark some of the interesting features. The feature V1 resembles the EVF observed at $l = 5.4°$ in Fig. 1. The feature V1 originates as the material on the 'overshooting' feature O1 (which has passed very close to the CMZ and brushed it) crashes onto the dust lane feature D1.

(v) is satisfied because colliding clouds are part of the general large-scale flow and so their velocities are always within the limits defined by the TVC. Property (vi) is satisfied because in our interpretation some of the features are naturally connected with the dust lanes.

With our existing simulation, we are not able to verify whether features formed in this way satisfy Property (iii). One of the unrealistic properties of our simulation is that the gas layer is too thin compared to observations (typical thickness of molecular gas in the simulations is only $H \sim 10$ pc), probably due to the lack of stellar feedback (see the discussion in section 5.5.1 of Sormani et al. 2018b). The thinness of the simulations can also be appreciated from the movies linked in the Supplementary Information section below. Hence, on scales much larger than ~ 10 pc, the gas is always more elongated in longitude than in latitude in our simulations, contrary to Property (iii). However, we might argue that both Property (iii) and (vii) may be expected for more realistic (and therefore more vertically 'puffed up') clouds within the context of our interpretation. When two clouds collide at high speed, we expect them to be compressed in the direction of motion (in this case, the l direction). This might explain Property (iii). Similarly, one might expect that a collision produces a strong compression shock on one side, visible as a sharp edge (Property vii).

The masses of the features in the simulations are comparable to the masses of the observed EVFs. For example. the mass of the feature V1 in the simulation is $\simeq 2.5 \times 10^6$ M$_\odot$ while the mass of the observed $l = 5.4°$ feature has been estimated by Liszt (2006) as $\simeq 5 \times 10^6$ M$_\odot$. This is a good agreement given that (a) the processes that produce the EVFs and therefore their masses are stochastic and (b) the masses measured from the observations are very uncertain due to the uncertainty in the CO-to-H$_2$ conversion factor ($X_{\rm CO}$). Indeed, standard assumptions made to calibrate $X_{\rm CO}$ such as virial equilibrium (e.g. Bolatto, Wolfire & Leroy 2013) are most likely not valid for the features considered here, which are in a highly dynamical environment.

As noted in Section 2 (Property viii), observed EVFs typically have a very complicated internal position–position–velocity (PPV) structure and break up into several sub-components with strong velocity gradients when observed at very high resolution. What is the small-scale structure of the EVFs obtained in the simulations? To investigate this, we show in Figs 6 and 7 the CO PPV maps of the features V1 and V2 studied above. Movies that show the same

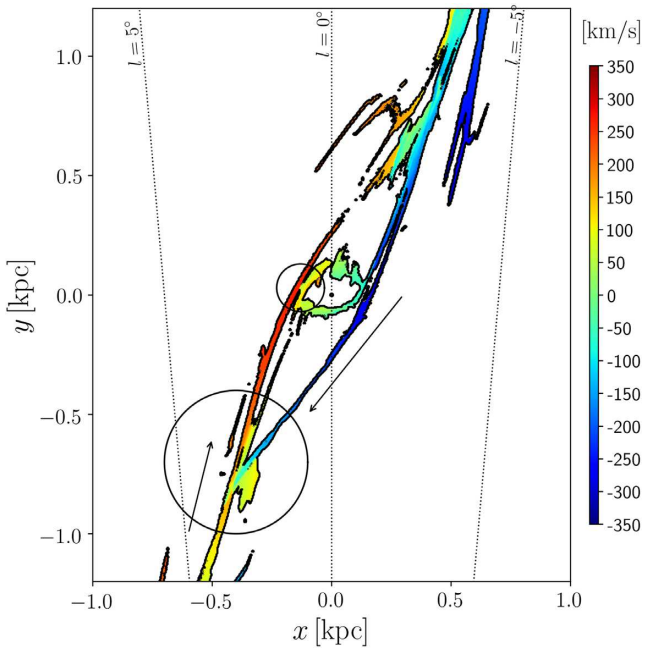

Figure 4. Line-of-sight velocity in the (x, y) plane. The larger circle highlights where the feature V1 shown in Fig. 3 originates. In this region, material with very different line-of-sight velocities collides, producing the large velocity dispersion observed in the (l, v) plane. The smaller circle highlights a region at the outer edges of the CMZ, where the dust lane brushes the CMZ. This behaviour also brings into contact material with very different velocities and can give rise to EVFs.

features from different orientations are also available at the link provided in the Supplementary Information section below. These show that V1 and V2 are indeed connected structures in 3D physical Position–Position–Position space and not coincidental amalgamations of unconnected components. The simulated EVFs possess a certain degree of internal structure (particularly the kinematical structure of V2 appears to be significantly more complex than of V1), but the real observed EVFs display a much higher degree of complexity (compare Figs 6 and 7 with figs. 6–9 of Liszt 2006 and fig. 30 of Longmore et al. 2017). This is not unexpected, given that our simulations start out very smooth and lack any kind of stellar feedback, self-gravity, and/or initial noise that could generate substructure, so that on small scales clouds tend be much smoother than their counterparts in the real Galaxy. It is, however, interesting to note that the simulated EVFs *do* have some substructure due to the unsteady gas flow caused by the bar, in contrast to the gas outside the bar region, which is extremely smooth.[4][5] Another aspect that is evident from Figs 6 and 7 is the small vertical extent (i.e. in the z direction) of our simulations discussed above. Despite these caveats, the comparison shows that the simulated EVFs may be identified with the bulk gas of the observed EVFs.

[4]The smoothness outside the bar region can be appreciated, for example in the visualization downloadable at the following link: https://doi.org/10.7910/DVN/XFDYY7/0EEVVX.

[5]The observations, as seen, for example in Longmore et al. (2017), also seem to indicate a possible connection between the statistics of the small-scale velocity structure and the type of EVF. Since our simulations are currently unable to reproduce the small-scale complexity of EVFs, we refrain from specifying the expected statistics of the different small-scale velocity structures. However, this is worth further study.

Finally, we note the following. In the previous section, we have identified two mechanisms that produce collisions (and therefore EVFs) in our simulations. The first is overshooting material that collides with the dust lanes on the opposite side, exemplified by feature V1 in Fig. 3. The second is material on the dust lanes that collides with CMZ material, exemplified by feature V2 in Fig. 5. However, we cannot exclude that in a more turbulent, realistic environment further mechanisms that generate collisions are possible. For example, multiple dust lanes are generally expected to be very close in real space although they have very different line-of-sight velocities. A relatively small perturbation to the velocity field (induced, for example by an external perturbation such as accretion from the circumgalactic medium or stellar feedback) may cause them to touch. This would lead to a transfer of material between the two (the faster dust lane is decelerated, while the slower one is accelerated), which in the (l, v) diagram would show up as an EVF. The key point is that velocity dispersions of the order of $\sim$ 100–200 km s^{-1} (comparable to the velocity of the Sun around the Galactic Centre) suggest that collisions between large-scale Galactic flows are involved. The presence of a bar creates the perfect environment to make such collisions likely.

5.1 Comparison with previous work

Compared to the other interpretations (a) to (d) listed in the introduction, we note the following. Unlike interpretation (a), according to which EVFs are extended structures that coincidentally line parallel to the line-of-sight, our interpretation does not suffer from the 'finger of god' effect. The patches of gas producing the EVFs in our simulations are always localized in (x, y) space and in general do not correspond to structures that are elongated along the line-of-sight. For example, we have verified that our features remain 'extended' in the (l, v) plane even if observed at different angles ϕ between the major axis of the bar and the Sun–GC line.

According to interpretation (b), magnetic instabilities alone (without a bar potential) are responsible for creating the EVFs. However, the synthetic (l, v) diagrams produced from simulations of this mechanism performed to date (Machida et al. 2009; Suzuki et al. 2015; Kakiuchi et al. 2018) do not seem to be able to convincingly reproduce the morphology of the EVFs in the (l, v) plane (Properties i and ii in Section 2). Moreover, in this interpretation, the connection with the dust lanes of the MW bar (Property vi in Section 2) remains unexplained. Nevertheless, it is possible that magnetic fields, when added on top of the bar potential, play a role in shaping the properties and morphologies of the EVFs.

Interpretation (c) assumes that EVFs are created by gravitational kicks around IMBHs. According to this interpretation, the large-velocity dispersion seen in an EVF should depend on the impact parameter of the incoming gas cloud relative to the IMBH and on the mass of the IMBH and should have no relation to the TVC and/or to the dust lanes features of the MW. Hence, in this interpretation, it is unclear why the EVFs never extend beyond the TVC at their longitudes (Property v) and why they seem to be associated with the dust lanes of the MW (Property vi). This interpretation also posits an ad hoc assumption, namely the presence of IMBHs, which is unnecessary since it can be avoided in our interpretation. Finally, we note that in the case of the CO-0.40-0.22 cloud, an EVF that has been claimed to be the signature of an IMBH close to the Galactic Centre (Oka et al. 2017), constraints on the radio spectrum and a detection of a mid-infrared point source both disfavour the presence of an IMBH (Ravi, Vedantham & Phinney 2018).

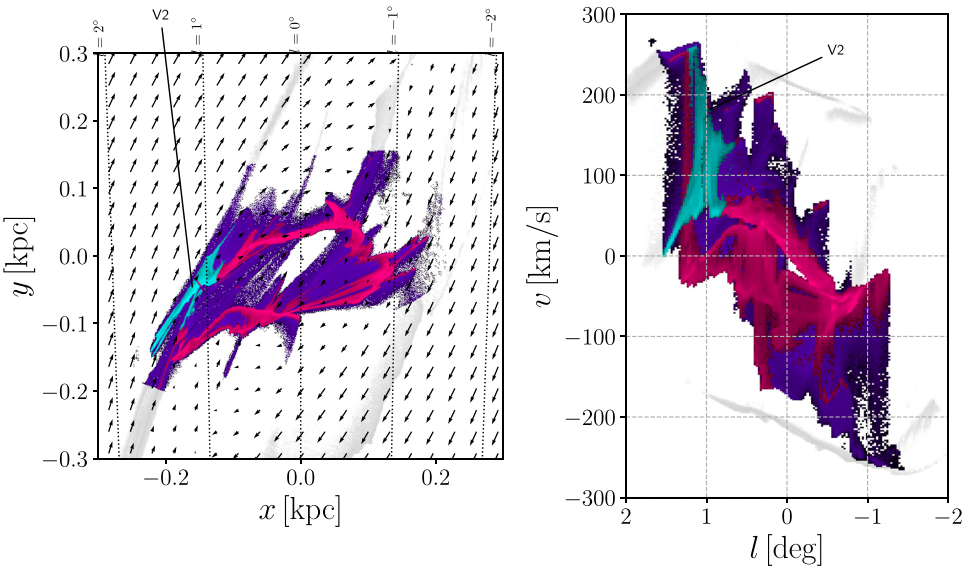

Figure 5. Features in the (x, y) plane and their projection to the (l, v) plane in the central regions for the simulation snapshot at $t = 191$ Myr. The feature V2 illustrates the second type of EVF. This is created as incoming material from the dust lanes crashes into the CMZ.

The interpretation (d) of Fux (1999) is essentially the same that we have given in this paper but in an embryonic state. The simulations of Fux (1999) did not possess the necessary resolution to actually see the EVFs in the synthetic (l, v) diagrams. Fux speculated about the implications of his simulations and imagined what he would have seen if he had higher resolution. We have refined the Fux (1999) interpretation by correcting some parts (e.g. the clumps are not really 'crossing' the dust lane and exiting on the other side as Fux suggested but instead are joining and merging with the dust lane and then flowing together towards the central regions) and filling in some details (e.g. the origin of some of the clumps hitting the dust lane is clumps from the dust lanes on the other side that have overshot).

5.2 Implications for the observations

In Section 4, we showed that we can distinguish two basic types of EVFs in the simulation. The first is produced by material on the dust lanes that collides with overshooting material from the other side. The second is produced by material on the dust lanes that collides with CMZ material.

In the observations, some features can be associated quite clearly with one or the other of these two possibilities. For example, the features at $l = 5.4^\circ$ and $l = 3.2^\circ$ in Fig. 1 are most likely of the first type (because of the way they are associated with the dust lane features L1–L3 and because their longitudes place them outside the CMZ), while the feature at $l = 1.3^\circ$ is most likely of the second type (because it connects with dense CMZ gas, see Fig. 1). Fig. 8 shows a sketch of how the geometry of the gas surrounding the CMZ might look like according to our interpretation. For other features in the observations, the situation is more ambiguous, and one needs to study this on a case-by-case basis, checking, for example the connection between them and other features such as dust lane features and using high-resolution data, which is outside the scope of the present paper.

The HI projection in Fig. 2 displays many features that cannot be seen in the CO projection. Thus, we expect that several features that are invisible in high-density tracers may be detected in low-density observational tracers such as HI (or the CO $J = 1 \rightarrow 0$ line observed with high enough sensitivity). The features identified in low-density tracers can be used to connect the features seen in higher density tracers such as NH_3 or HCN. This will be necessary to get a complete picture of the 3D geometry and gas flows in and around the CMZ.

Finally, it is worth noting that if our interpretation of the $l = 5.4^\circ$ and $l = 3.2^\circ$ EVFs is correct, we are directly witnessing collisions at a relative speed of $\Delta v \sim 200\,\mathrm{km\,s^{-1}}$. This is a perfect laboratory for studying what happens when two molecular clouds with masses in excess of $M = 10^6\,\mathrm{M}_\odot$ collide with each other with extreme velocities. We expect to find a rich chemistry and the presence of shock tracers associated with these features in the observations. If the interpretation of the $l = 1.3^\circ$ EVF is correct, we are directly witnessing material that is accreting onto the CMZ. Studying this feature in more detail can, therefore, give insight on the process of accretion as it is happening and on the physical and chemical condition of the accreted gas.

6 SUMMARY

Surrounding the Galactic Centre, there exist an enigmatic population of compact molecular clouds with extreme velocity dispersions. These EVFs dominate the kinematics of gas just outside the CMZ. We have used hydrodynamical simulations of gas flow in a barred potential to interpret these clouds. We have found that similar features occur naturally in these simulations. They originate from collisions between material that is falling along the dust lanes of the bar and material with substantially different line-of-sight velocities. We have distinguished between two types:

(i) EVFs like the feature V1 in Fig. 3, which originate from the collision between material on the dust lanes and material that has 'overshot' from the dust lane on the opposite side;

(ii) EVFs like the feature V2 in Fig. 5, which originate from the collision between material on the dust lanes and material belonging to the CMZ.

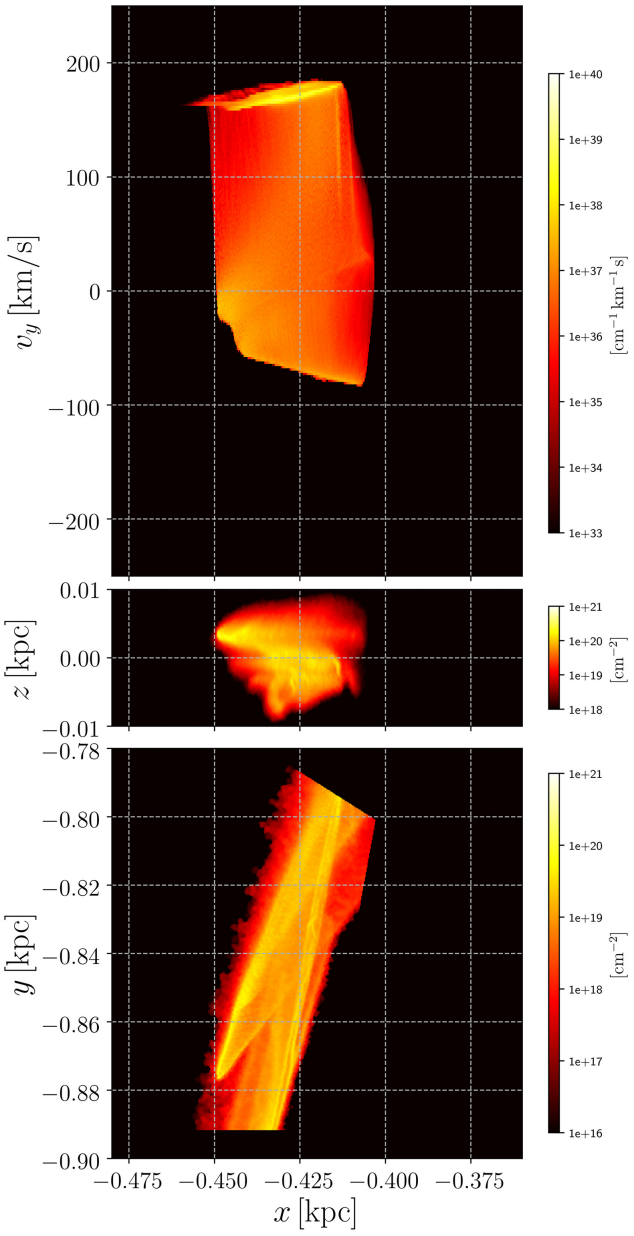

Figure 6. Zoom-in that shows the 3D CO position–position–velocity structure of the feature V1 in Fig. 3. A movie showing the feature from different orientations can be downloaded from https://doi.org/10.7910/DVN/XFDYY7/QXMRGO.

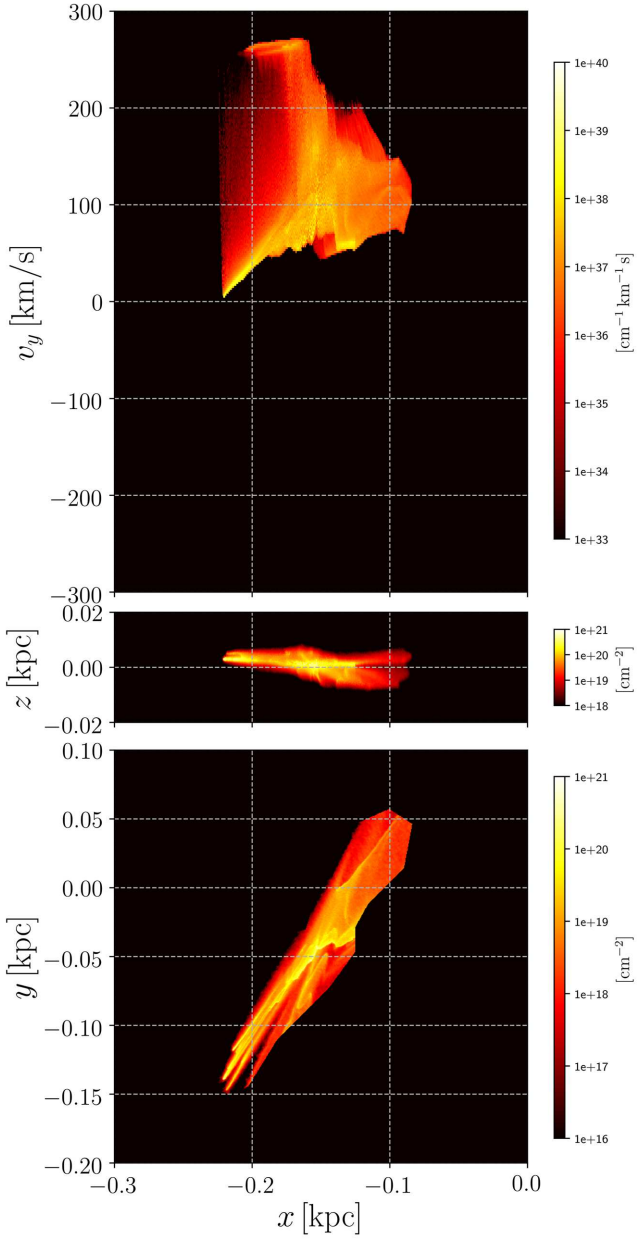

Figure 7. Zoom-in that shows the 3D CO position–position–velocity structure of the feature V2 in Fig. 5. A movie showing the feature from different orientations can be downloaded from https://doi.org/10.7910/DVN/XFDYY7/XRNIAD.

Examples of both types of features can be identified in the observations. The sketch in Fig. 8 shows our proposed interpretation of the most unambiguous features. Other features can be identified in the data, but the interpretation is more ambiguous and will require more careful analysis with higher resolution observations.

If our interpretation is correct, we are witnessing clouds colliding at relative velocities of $\Delta v \sim 200\,\mathrm{km\,s^{-1}}$ (e.g. the $l = 5.4^\circ$ and $l = 3.2^\circ$ clouds). This provides an excellent laboratory to study extreme cloud collisions. We are also directly witnessing gas being accreted onto the CMZ (e.g. the $l = 1.3^\circ$ cloud). This provides a unique opportunity to study how gas is accreted and the physical and chemical properties of the accreted gas.

ACKNOWLEDGEMENTS

MCS thanks Tom Dame and Harvey Liszt for insightful comments and discussions. We thank Jean-charles Lambert for developing GLNEMO2, a freely distributed interactive visualization 3D software for *N*-body snapshots that is publicly available at the following link: https://projets.lam.fr/projects/glnemo2. MCS, RGT, SCOG, and RSK acknowledge support from the Deutsche Forschungsgemeinschaft via the Collaborative Research Centre (SFB 881) 'The Milky Way System' (subprojects B1, B2, and B8) and the Priority Program SPP 1573 'Physics of the Interstellar Medium' (grant numbers KL 1358/18.1, KL 1358/19.2, and GL 668/2-1). RSK furthermore thanks the European Research Council for funding in the ERC Advanced Grant STARLIGHT (project number 339177). ATB

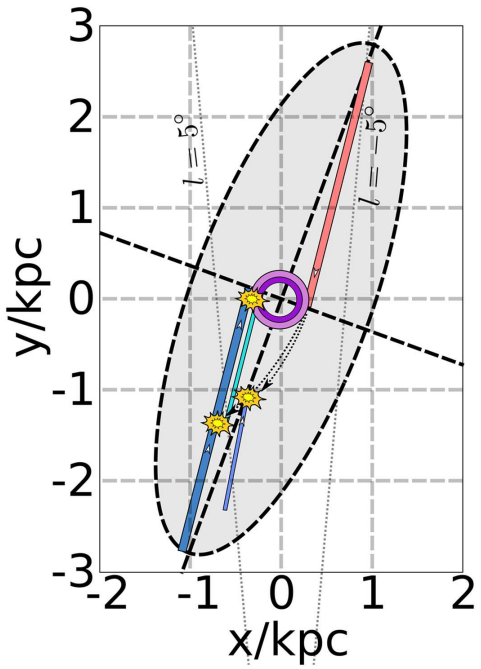

Figure 8. Sketch of how the geometry of the gas surrounding the CMZ might look like according to our interpretation. Coloured straight lines represent the various dust lanes of the MW. The purple circle represents the CMZ. The two yellow clouds on the near-side dust lanes represent the $l = 5.4°$ and $l = 3.2°$ (aka Bania Clump 2) EVFs in Fig. 1, respectively. The yellow cloud at the intersection between dust lanes and CMZ represents the $l = 1.3°$ EVF in Fig. 1.

would like to acknowledge the funding provided from the European Union's Horizon 2020 research and innovation programme (grant agreement No 726384). CDB and HPC gratefully acknowledge support for this work from the National Science Foundation under Grant No. (1816715). PCC acknowledges support from the Science and Technology Facilities Council (under grant ST/N00706/1) and StarFormMapper, a project that has received funding from the European Union's Horizon 2020 Research and Innovation Programme, under grant agreement no. 687528. HPH thanks the LSSTC Data Science Fellowship Program, which is funded by LSSTC, NSF Cybertraining Grant No. 1829740, the Brinson Foundation, and the Moore Foundation; his participation in the program has benefited this work. RJS gratefully acknowledges an STFC Ernest Rutherford fellowship (grant ST/N00485X/1) and HPC from the Durham DiRAC supercomputing facility (grants ST/P002293/1, ST/R002371/1, ST/S002502/1, and ST/R000832/1). The authors acknowledge support by the state of Baden-Württemberg through bwHPC and the German Research Foundation (DFG) through grant INST 35/1134-1 FUGG.

REFERENCES

Baba J., Saitoh T. R., Wada K., 2010, PASJ, 62, 1413
Binney J., Merrifield M., 1998, Galactic Astronomy. Princeton Univ. Press, Princeton, NJ
Bitran M., Alvarez H., Bronfman L., May J., Thaddeus P., 1997, A&AS, 125, 99
Bland-Hawthorn J., Gerhard O., 2016, ARA&A, 54, 529
Bolatto A. D., Wolfire M., Leroy A. K., 2013, ARA&A, 51, 207
Boyce P. J., Cohen R. J., 1994, A&AS, 107, 563
Boyce P. J., Cohen R. J., Dent W. R. F., 1989, MNRAS, 239, 1013
Clark P. C., Glover S. C. O., Klessen R. S., 2012, MNRAS, 420, 745
Clark P. C., Glover S. C. O., Ragan S. E., Shetty R., Klessen R. S., 2013, ApJ, 768, L34
Draine B. T., 1978, ApJS, 36, 595
Fujishita M. et al., 2009, PASJ, 61, 1039
Fukui Y. et al., 2006, Science, 314, 106
Fux R., 1999, A&A, 345, 787
Gilmore G., Reid N., 1983, MNRAS, 202, 1025
Glover S. C. O., Clark P. C., 2012, MNRAS, 421, 116
Glover S. C. O., Mac Low M.-M., 2007a, ApJS, 169, 239
Glover S. C. O., Mac Low M.-M., 2007b, ApJ, 659, 1317
Glover S. C. O., Federrath C., Mac Low M.-M., Klessen R. S., 2010, MNRAS, 404, 2
Goldsmith P. F., Langer W. D., 1978, ApJ, 222, 881
Henshaw J. D. et al., 2016, MNRAS, 457, 2675
Heyer M., Dame T. M., 2015, ARA&A, 53, 583
Jones P. A. et al., 2012, MNRAS, 419, 2961
Kakiuchi K., Suzuki T. K., Fukui Y., Torii K., Enokiya R., Machida M., Matsumoto R., 2018, MNRAS, 476, 5629
Kalberla P. M. W., Dedes L., 2008, A&A, 487, 951
Kruijssen J. M. D., Dale J. E., Longmore S. N., 2015, MNRAS, 447, 1059
Launhardt R., Zylka R., Mezger P. G., 2002, A&A, 384, 112
Lee C. W., Lee H. M., Ann H. B., Kwon K. H., 1999, ApJ, 513, 242
Liszt H. S., 2006, A&A, 447, 533
Liszt H. S., 2008, A&A, 486, 467
Longmore S. N. et al., 2017, MNRAS, 470, 1462
Machida M. et al., 2009, PASJ, 61, 411
Marshall D. J., Fux R., Robin A. C., Reylé C., 2008, A&A, 477, L21
McClure-Griffiths N. M., Dickey J. M., Gaensler B. M., Green A. J., Green J. A., Haverkorn M., 2012, ApJS, 199, 12
McMillan P. J., 2017, MNRAS, 465, 76
Mizuno A., Fukui Y., 2004, in Clemens D., Shah R., Brainerd T., eds, ASP Conf. Ser, Vol. 317, Milky Way Surveys: The Structure and Evolution of our Galaxy, Astron. Soc. Pac., San Francisco,p. 59
Molinari S. et al., 2011, ApJ, 735, L33
Navarro J. F., Frenk C. S., White S. D. M., 1996, ApJ, 462, 563
Nelson R. P., Langer W. D., 1997, ApJ, 482, 796
Oka T., Hasegawa T., Sato F., Tsuboi M., Miyazaki A., 1998, ApJS, 118, 455
Oka T., Onodera Y., Nagai M., Tanaka K., Matsumura S., Kamegai K., 2012, ApJS, 201, 14
Oka T., Mizuno R., Miura K., Takekawa S., 2016, ApJ, 816, L7
Oka T., Tsujimoto S., Iwata Y., Nomura M., Takekawa S., 2017, Nat. Astron., 1, 709
Parker E. N., 1966, ApJ, 145, 811
Portail M., Gerhard O., Wegg C., Ness M., 2017, MNRAS, 465, 1621
Ravi V., Vedantham H., Phinney E. S., 2018, MNRAS, 478, L72
Ridley M. G. L., Sormani M. C., Treß R. G., Magorrian J., Klessen R. S., 2017, MNRAS, 469, 2251
Riquelme D. et al., 2018, A&A, 613, A42
Sandage A., 1961, The Hubble Atlas of Galaxies. Carnegie Institution of Washington, Washington, D.C.
Sanders J. L., Smith L., Evans N. W., 2019, MNRAS, preprint (arXiv: 1903.02009)
Sormani M. C., Barnes A. T., 2019, MNRAS, 484, 1213
Sormani M. C., Binney J., Magorrian J., 2015a, MNRAS, 449, 2421
Sormani M. C., Binney J., Magorrian J., 2015b, MNRAS, 454, 1818
Sormani M. C., Sobacchi E., Fragkoudi F., Ridley M., Treß R. G., Glover S. C. O., Klessen R. S., 2018a, MNRAS, 481, 2
Sormani M. C., Treß R. G., Ridley M., Glover S. C. O., Klessen R. S., Binney J., Magorrian J., Smith R., 2018b, MNRAS, 475, 2383
Springel V., 2010, MNRAS, 401, 791
Stark A. A., Bania T. M., 1986, ApJ, 306, L17
Suzuki T. K., Fukui Y., Torii K., Machida M., Matsumoto R., 2015, MNRAS, 454, 3049
Takekawa S., Oka T., Iwata Y., Tsujimoto S., Nomura M., 2019a, ApJ, 871, L1

Takekawa S., Oka T., Tokuyama S., Tanabe K., Iwata Y., Tsujimoto S., Nomura M., Shibuya Y., 2019b, preprint (arXiv:1903.08896)
Torii K. et al., 2010, PASJ, 62, 1307

SUPPORTING INFORMATION

Supplementary data are available at *MNRAS* online.

flyby.mp4
lv02.mp4
lv12.mp4
zoomV1.mp4
zoomV2.mp4

Please note: Oxford University Press is not responsible for the content or functionality of any supporting materials supplied by the authors. Any queries (other than missing material) should be directed to the corresponding author for the article.

APPENDIX A: GRAVITATIONAL POTENTIAL

We employ a realistic external gravitational potential that is the sum of four components: bar, bulge, disc, and halo. The axisymmetric part is derived from the work of McMillan (2017), whose potential is created to fit observational constraints and to be consistent with expectations from theoretical modelling of the Milky Way as a whole. The bar and the bulge are built to be consistent with observational constraints from near-infrared photometry (Launhardt, Zylka & Mezger 2002) and with dynamical constraints on the quadrupole of the bar (Sormani et al. 2015b; see also Ridley et al. 2017). The bar rotates with a constant pattern speed of $\Omega_p = 40\,\mathrm{km\,s^{-1}\,kpc^{-1}}$. The axisymmetric part (the velocity curve) and the first few multipoles are shown in Figs A1 and A2. The details of each component of the potential are as follows.

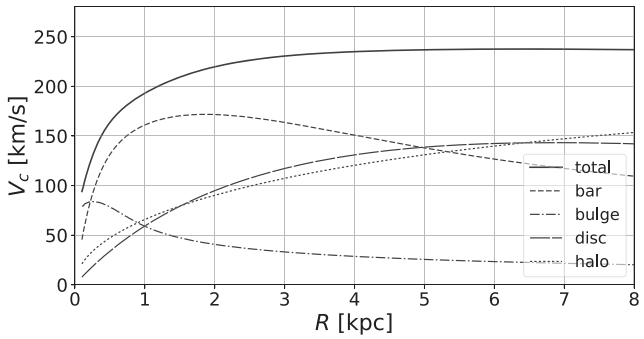

Figure A1. The circular velocity curve in the plane $z = 0$ for the potential used in this paper. The separate contributions from bar, bulge, disc, and halo are also shown.

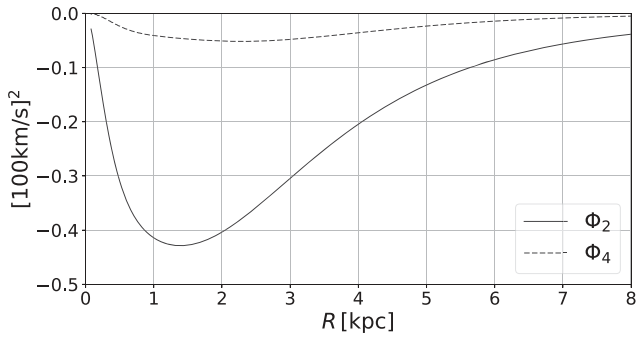

Figure A2. The quadrupole Φ_2 and octupole Φ_4 in the plane $z = 0$ for the potential used in this paper. These are defined by the multipole expansion of the potential in the plane of the Galaxy, $\Phi(R, \phi) = \Phi_0(R) + \sum_{m=1}^{\infty} \Phi_m(R) \cos(m\phi + \phi_m)$ where ϕ_m are constants and $\{R, \phi, z\}$ denote standard cylindrical coordinates.

Bulge. This component is generated by the following density distribution:

$$\rho_b = \frac{\rho_{b0}}{(1 + a/a_0)^{\alpha}} \exp\left[-(a/a_{cut})^2\right] \tag{A1}$$

where

$$a = \sqrt{x^2 + y^2 + \frac{z^2}{q_b^2}}. \tag{A2}$$

We use the following parameters: $\alpha = 1.8$, $\rho_{b0} = 9.5 \times 10^4\,\mathrm{M_\odot\,pc^{-3}}$, $a_{cut} = 0.5\,\mathrm{kpc}$, $q_b = 0.5$, and $a_0 = 10^{-3}\,\mathrm{kpc}$.

Bar. The density of the bar is taken to be:

$$\rho_B = \rho_{B1} \exp(-a_1/a_{B1}) + \rho_{B2} \exp(-a_2/a_{B2}), \tag{A3}$$

where

$$a_1 = \sqrt{x^2 + \frac{y^2+z^2}{q_{B1}^2}}, \tag{A4}$$

$$a_2 = \sqrt{x^2 + \frac{y^2+z^2}{q_{B2}^2}}. \tag{A5}$$

We use the following values for the parameters: $\rho_{B1} = 16\,\mathrm{M_\odot\,pc^{-3}}$, $a_{B1} = 0.3\,\mathrm{kpc}$, $q_{B1} = 0.5$, $\rho_{B2} = 3\,\mathrm{M_\odot\,pc^{-3}}$, $a_{B2} = 1\,\mathrm{kpc}$, and $q_{B2} = 0.5$.

Disc. The disc is the sum of a thick and a thin disc (Gilmore & Reid 1983). The density distribution is:

$$\rho_d = \frac{\Sigma_1}{2z_1} \exp\left(-\frac{|z|}{z_1} - \frac{R}{R_{d1}}\right) + \frac{\Sigma_2}{2z_2} \exp\left(-\frac{|z|}{z_2} - \frac{R}{R_{d2}}\right), \tag{A6}$$

where $\Sigma_1 = 572\,\mathrm{M_\odot\,kpc^{-2}}$, $R_{d1} = 2.9\,\mathrm{kpc}$, $z_1 = 0.3\,\mathrm{kpc}$, $\Sigma_2 = 147\,\mathrm{M_\odot\,kpc^{-2}}$, $R_{d2} = 3.31\,\mathrm{kpc}$, and $z_2 = 0.9\,\mathrm{kpc}$.

Halo. This is a simple Navarro, Frenk & White (1996) profile. The density distribution is:

$$\rho_h = \frac{\rho_{h0}}{x(1+x)^2}, \tag{A7}$$

where $x = r/r_h$, $r = (x^2 + y^2 + z^2)^{1/2}$, $\rho_{h0} = 0.00846\,\mathrm{M_\odot\,pc^{-3}}$, and $r_h = 20.2\,\mathrm{kpc}$.

This paper has been typeset from a TEX/LATEX file prepared by the author.